Delft University of Technology

Document Version
Final published version

Licence
CC BY

Citation (APA)
Eidi, A., & Dwight, R. P. (2026). A surrogate-based Bayesian framework for parametric calibration of URANS turbulence models informed by anisotropic pressure fluctuations. *Flow, Turbulence and Combustion*, *117*(1), Article 1. https://doi.org/10.1007/s10494-026-00763-x

Flow, Turbulence and Combustion (2026) 117:1
https://doi.org/10.1007/s10494-026-00763-x

RESEARCH

A surrogate-based Bayesian framework for parametric calibration of URANS turbulence models informed by anisotropic pressure fluctuations

Ali Eidi[1] · **Richard P. Dwight**[1]

Received: 30 January 2026 / Revised: 14 May 2026 / Accepted: 19 May 2026

Abstract

Flow-induced vibrations in wall-bounded flows remain a major challenge in many engineering applications. While fully predictive turbulence-induced vibration simulations generally require scale-resolving approaches, unsteady Reynolds-averaged Navier–Stokes (URANS) methods are employed in practice due to their favorable computational cost. However, their predictive reliability is limited by uncertainty in turbulence-model parameters, structural model–form error, and deficiencies in representing turbulent fluctuations. This work presents a surrogate-based Bayesian calibration framework for the SST k–ω model, incorporating anisotropic pressure-fluctuation reconstruction to quantify and reduce model uncertainty. Global Sobol' sensitivity analysis, surrogate modeling, and Bayesian inference are combined to identify influential parameters and assimilate high-fidelity reference data. The framework is applied to turbulent channel flow, turbulent annular flow, and a blunt-end cantilevered-rod configuration. Across all cases, the specific dissipation-rate coefficient $\alpha_{\omega 1}$ and the turbulent kinetic-energy dissipation coefficient β^* consistently dominate variability in mean-flow quantities and reconstructed fluctuation statistics. Bayesian calibration constrains these parameters to consistent regions of the admissible space, while less influential coefficients remain weakly informed. Gaussian process regression and polynomial chaos expansion surrogates yield nearly identical posterior and predictive distributions, demonstrating robustness to surrogate choice. Remaining discrepancies with reference data are attributed primarily to structural turbulence model limitations rather than parametric uncertainty.

Keywords Uncertainty quantification · Sensitivity analysis · URANS model calibration · Flow-induced vibrations · Surrogate modeling

---

Ali Eidi
a.eidi@tudelft.nl

Richard P. Dwight
r.p.dwight@tudelft.nl

[1] Department of Flow Physics and Technology, TU Delft, Kluyverweg 1, Delft 2629HS, Netherlands

1 Introduction

Turbulence-induced vibration (TIV) and flow-induced vibration (FIV) represent critical challenges in the design and safe operation of nuclear fuel assemblies and other engineering structures exposed to turbulent flows. In nuclear reactors, axial coolant flows generate unsteady pressure and velocity fluctuations that excite structural components, potentially causing long-term fretting wear, fatigue, and compromised integrity (Shu et al. 2019). Accurate prediction of these fluctuating loads is therefore essential for ensuring structural reliability and extending component service life.

Fluid–structure interaction (FSI) simulations are widely employed to investigate TIV phenomena. Although scale-resolving methods such as direct numerical simulation (DNS) and large eddy simulation (LES) offer detailed resolution of turbulent fluctuations, their prohibitive computational cost renders them impractical for routine industrial FSI analyses. Consequently, unsteady Reynolds-averaged Navier–Stokes (URANS) simulations remain the predominant tool in engineering practice (De Ridder et al. 2013). However, URANS predictions are fundamentally constrained by the employed turbulence closure models, especially for quantities involving turbulent fluctuations and unsteady forcing.

To improve URANS-based predictions without resolving all turbulent scales, pressure-fluctuation reconstruction models have been developed to recover unresolved pressure statistics from URANS fields (Smirnov et al. 2001; Kottapalli et al. 2017). The anisotropic pressure fluctuation model (AniPFM) advances this approach by incorporating anisotropic velocity fluctuations, yielding enhanced pressure-field predictions in configurations relevant to TIV (Zwijsen et al. 2024a, b). Nevertheless, URANS–AniPFM predictions exhibit substantial sensitivity to turbulence model parameters, and accurate reproduction of turbulence statistics is not assured within standard parameter ranges. This sensitivity underscores the need for systematic uncertainty quantification (UQ) and calibration of turbulence model parameters.

Uncertainties in RANS and URANS predictions arise not only from unresolved turbulent fluctuations but also from the turbulence-closure models themselves (Xiao and Cinnella 2019). Widely used closures, such as the SST k–ω model (Menter 1994), rely on empirically tuned coefficients that are typically calibrated using canonical flow configurations (Duraisamy et al. 2019). When applied to complex geometries or flow conditions outside their calibration envelope, these coefficients may deviate from optimal values, leading to significant model–form uncertainty (Eidi et al. 2021, 2022). Within a Bayesian framework, turbulence model calibration is naturally posed as an inverse statistical problem, in which prior knowledge of closure parameters is updated using observational data to obtain posterior probability distributions (Cheung et al. 2011; Oliver and Moser 2011; Edeling et al. 2014; Margheri et al. 2014). Crucially, even optimally calibrated RANS models remain structurally imperfect representations of turbulent flows, such that residual discrepancies with reference data are generally unavoidable and should be interpreted in terms of intrinsic model–form error (Kennedy and O'Hagan 2001).

In this context, global sensitivity analysis (SA), surrogate modeling, and Bayesian inference provide complementary tools for turbulence model UQ: SA identifies the most influential closure parameters, surrogate models enable efficient uncertainty propagation for computationally expensive solvers, and Bayesian inference assimilates high-fidelity reference data to quantify posterior parameter uncertainty and predictive credibility (Xiao and Cinnella 2019). These approaches have been applied to calibrate SST and related turbulence models across a range of flow regimes (Hosder et al. 2007, 2010; Georgiadis and Yoder 2013; Schaefer et al. 2017; Erb and Hosder 2018; Zhao et al. 2018, 2019; Da Ronch et al. 2020; Subbian et al. 2020; Di Stefano et al. 2021; Jp et al. 2021; Li et al. 2022; Qiu et al. 2026). However, most existing studies remain limited to individual configurations or isolated calibration exercises, and unified surrogate-accelerated Bayesian UQ frameworks spanning multiple levels of geometric and physical complexity relevant to TIV and FSI applications are still scarce.

The present study bridges this gap by developing a comprehensive Bayesian UQ framework for turbulence model parameter uncertainty in URANS simulations augmented with pressure-fluctuation modeling. The key novelty lies in the combination of (i) surrogate-accelerated global SA, (ii) Bayesian calibration across multiple canonical and application-relevant flow configurations, and (iii) the explicit integration of anisotropic pressure-fluctuation reconstruction to inform turbulence model calibration with respect to fluctuation-driven quantities. The framework is applied consistently to three configurations of progressively increasing complexity: turbulent channel flow, turbulent annular flow, and a blunt-end cantilevered-rod geometry. These cases provide a systematic progression from canonical wall-bounded turbulence to a representative FSI-relevant application, enabling transfer of parameter sensitivity information from inexpensive auxiliary flows to a computationally prohibitive geometry. The analysis centers on the SST k–ω model and targets quantities of interest (QoIs) directly relevant to unsteady loading and TIV, including mean-flow statistics, turbulent kinetic energy, and pressure-fluctuation intensity.

The remainder of the paper is organized as follows. Section 2 outlines the UQ methodology. Section 3 describes the three flow cases and presents the corresponding SA, Bayesian calibration, and predictive uncertainty results. Conclusions are drawn in Section 4.

2 Methodology

This section outlines the UQ framework employed in the present study. The methodology comprises four primary components: (i) global sensitivity analysis for parameter screening, (ii) surrogate modeling to enable efficient uncertainty propagation, (iii) Bayesian calibration via Markov-chain Monte Carlo (MCMC) sampling, and (iv) definition of the admissible turbulence model parameter space. In addition, the AniPFM used to reconstruct unresolved turbulent pressure fluctuations from URANS mean fields is described in a dedicated subsection.

2.1 Sensitivity analysis framework

Global SA is used to screen and rank turbulence model parameters according to their contribution to output variability. A variance-based, non-intrusive Sobol' methodology is adopted (Saltelli et al. 2008), whereby uncertainty is introduced exclusively through the model inputs while the governing equations, numerical schemes, and solver settings are held fixed. Each turbulence model parameter is assigned a bounded interval based on literature-reported values, defining a hyper-rectangular parameter space. Sampling is performed using a Saltelli extension of Sobol' low-discrepancy sequences, as implemented in the `SALib` library (Herman and Usher 2017). For a parameter space of dimension d, this sampling strategy requires

$$N_{\mathrm{SA}} = N\,(2d+2) \tag{1}$$

model evaluations, where N denotes the base sample size, i.e. the number of samples used to construct each independent Sobol' sampling matrix. This formulation enables efficient and unbiased estimation of first-order Sobol' indices while maintaining good space-filling properties.

Sensitivity is quantified using first-order Sobol' indices,

$$S_i = \frac{\mathrm{Var}(\mathbb{E}[\,Y \mid \theta_i\,])}{\mathrm{Var}(Y)}, \tag{2}$$

which measure the isolated contribution of parameter θ_i to the total variance of a QoI Y. In practice, the conditional expectations and variances are estimated using Monte Carlo sampling based on a Saltelli sampling design. For each QoI, the model response Y is evaluated at a finite set of sampled parameter realizations, and the required statistics are approximated from the resulting ensemble of model outputs. Indices are computed independently for each QoI and, where relevant, at each spatial location. Restricting the analysis to first-order indices provides an effective and computationally tractable screening tool, sufficient for identifying dominant turbulence model parameters in the present context. For configurations where direct CFD-based SA is computationally prohibitive, the same Sobol' framework is applied to surrogate models trained on a reduced set of simulations, enabling consistent parameter ranking at negligible additional cost.

2.2 Surrogate modeling approaches

Surrogate models are introduced to replace repeated CFD evaluations during uncertainty propagation and Bayesian inference. The surrogate approximates the parameter-to-output mapping

$$\boldsymbol{\theta} \in \mathbb{R}^M \;\mapsto\; \mathbf{y}(\boldsymbol{\theta}) \in \mathbb{R}^P, \tag{3}$$

where $\boldsymbol{\theta}$ denotes the vector of M uncertain turbulence model parameters and $\mathbf{y}$ collects the P corresponding QoIs, such as mean-flow variables and turbulence statistics evaluated at multiple spatial locations.

Surrogate construction is performed after global SA using only the parameters identified as influential, thereby reducing the effective dimensionality of the input space and improving surrogate robustness and accuracy. Training data are generated using Latin hypercube sampling (LHS) (McKay et al. 2000) in the reduced parameter space. Sobol' low-discrepancy sampling is employed exclusively for global SA, as it provides the structured sample sets required for consistent estimation of variance-based sensitivity indices. In contrast, LHS is preferred for surrogate construction because of its superior space-filling properties, enabling accurate interpolation with a limited number of training points. All surrogates are trained on standardized inputs and outputs.

2.2.1 Gaussian process regression

Gaussian process regression (GPR) (Williams and Rasmussen 2006), also known as Kriging, is employed as the primary surrogate-modeling technique. Each QoI is modeled independently as

$$y_j(\boldsymbol{\theta}) = \hat{y}_j(\boldsymbol{\theta}) + \varepsilon_j, \tag{4}$$

where $\hat{y}_j(\boldsymbol{\theta})$ denotes the surrogate prediction of the URANS model response and ε_j represents a stochastic discrepancy term accounting for residual model inadequacy and unresolved numerical effects. Following the Bayesian model-discrepancy framework of Kennedy and O'Hagan (2001), this discrepancy is assumed to be Gaussian with zero mean and variance estimated from residual analysis against reference data. This formulation allows parametric uncertainty to be distinguished from structural model-form uncertainty without introducing additional surrogate models. The deterministic surrogate is defined by a zero-mean Gaussian process with a squared-exponential covariance kernel,

$$k(\boldsymbol{\theta}, \boldsymbol{\theta}') = C \exp\left(-\frac{\|\boldsymbol{\theta} - \boldsymbol{\theta}'\|^2}{2l^2}\right) + \sigma_n^2 \delta_{\boldsymbol{\theta}\boldsymbol{\theta}'}, \tag{5}$$

with hyperparameters identified by maximizing the marginal log-likelihood.

Residuals between CFD outputs and the deterministic surrogate are modeled using an independent GPR, representing model inadequacy and unresolved numerical effects. During Bayesian inference, the corrected prediction $\tilde{y}_j = \hat{y}_j + \hat{r}_j$ is used inside the likelihood. Multi-output surrogates are constructed by grouping independently trained scalar GPs.

2.2.2 Polynomial chaos expansion

The Polynomial Chaos Expansion (PCE) (Ghanem and Spanos 1991; Xiu and Karniadakis 2002) is employed as an alternative surrogate for the cantilevered-rod case. The retained turbulence model parameters are mapped from their physical bounds to independent standardized variables $\boldsymbol{\xi} \in [-1, 1]^d$, consistent with uniform prior distributions. Each QoI is approximated as

$$y(\boldsymbol{\theta}) \approx \sum_{\boldsymbol{\alpha} \in \mathcal{A}} c_{\boldsymbol{\alpha}} \, \Psi_{\boldsymbol{\alpha}}(\boldsymbol{\xi}), \tag{6}$$

where $\Psi_{\boldsymbol{\alpha}}$ denotes multivariate Legendre polynomials and $\mathcal{A}$ a total-order truncated basis. Coefficients are identified via regularized least squares, and the polynomial order is selected using K-fold cross-validation. PCE enables efficient surrogate-based uncertainty propagation and analytical evaluation of output variance and Sobol' indices.

2.3 Bayesian inference framework

Bayesian inference is employed to quantify uncertainty in turbulence model parameters by combining prior information, surrogate-model predictions, and reference data within a probabilistic framework (Kennedy and O'Hagan 2001). All inference steps are carried out in the reduced parameter space identified by the global SA, thereby limiting the calibration to influential model coefficients.

The Bayesian calibration problem is formulated as an inverse statistical problem in which discrepancies between surrogate predictions and reference data are interpreted through a likelihood model. The likelihood is defined in a normalized output space to ensure balanced treatment of multiple QoIs. For GPR, the forward model entering the likelihood consists of the deterministic surrogate prediction augmented by an explicit model-inadequacy correction. Prior to sampling, residual analysis is performed to estimate observation-noise variances, either globally or per output, which are subsequently smoothed and mapped back to physical units.

Under the assumption of independent Gaussian errors, the resulting likelihood function is multivariate normal with diagonal covariance,

$$\log p(\mathbf{y} \mid \boldsymbol{\theta}) = -\frac{1}{2} \sum_i \left[\left(\frac{y_i - \hat{y}_i(\boldsymbol{\theta})}{\sigma_i} \right)^2 + \log(2\pi\sigma_i^2) \right]. \tag{7}$$

Uniform prior distributions are assigned over the admissible parameter domain, defined a priori based on physically and empirically justified ranges for the SST model coefficients (see Sect 2.4). Posterior sampling is performed using an Adaptive Metropolis algorithm (Haario et al. 2001), with proposals outside this admissible region rejected automatically. Posterior predictive distributions are obtained by propagating posterior samples through the surrogate model using Monte Carlo sampling.

By replacing repeated CFD evaluations with a computationally inexpensive surrogate, this framework enables efficient Bayesian calibration and predictive UQ while preserving consistency with the underlying URANS model response.

2.4 Turbulence modeling: parameter set

All simulations in this study employ the SST k–ω turbulence model (Menter 1994), which combines near-wall k–ω behavior with outer-layer k–ε characteristics through blending functions. The present work focuses on uncertainty in the closure coefficients entering the transport equations for the turbulent kinetic energy k and the specific dissipation rate ω.

Rather than repeating the full SST formulation, which is well established in the literature, we briefly summarize the model structure and explicitly identify the coefficients treated as uncertain. The SST model solves transport equations of the generic

from

$$\frac{\partial(\rho\phi)}{\partial t} + \frac{\partial(\rho u_j \phi)}{\partial x_j} = \mathcal{P}_\phi - \mathcal{D}_\phi + \frac{\partial}{\partial x_j}\left[\left(\mu + \frac{\mu_t}{\sigma_\phi}\right)\frac{\partial \phi}{\partial x_j}\right], \tag{fromd8}$$

where $\phi \in \{k, \omega\}$, $\mathcal{P}_\phi$ and $\mathcal{D}_\phi$ denote production and dissipation terms, and μ_t is the eddy viscosity. The latter is given by

$$\mu_t = \frac{\rho a_1 k}{\max(a_1 \omega,\, S F_2)}, \tag{9}$$

with F_2 a blending function and S the strain-rate magnitude. The complete governing equations and blending functions are provided in (Menter 1994).

The SST model contains nine independent closure coefficients governing production, diffusion, dissipation, and eddy-viscosity limitation. These coefficients define the full uncertainty space for the initial global SA. Nominal values and admissible sampling intervals are summarized in Table 1, based on literature-reported ranges (Zhang et al. 2022), and are used as uniform prior support in all subsequent analyses. The coefficients γ_1 and γ_2 are functions of β_1, β_2, β^*, $\alpha_{\omega 1}$, $\alpha_{\omega 2}$, and κ and enforce correct near-wall scaling and dissipation behavior. They are therefore not treated as independent uncertain parameters.

The nine coefficients in Table 1 constitute the full parameter space for the initial SA. Based on the resulting Sobol' indices, a reduced subset of influential parameters is retained for surrogate modeling and Bayesian calibration, while the complete formulation defines the physically consistent closure used in all CFD simulations.

2.5 Anisotropic pressure fluctuation model

The anisotropic pressure fluctuation model (AniPFM) (Zwijsen et al. 2024a, b) is employed to reconstruct unresolved pressure fluctuations from URANS solutions, enabling the estimation of unsteady loading relevant for TIV and FIV. AniPFM augments URANS by introducing synthetic, space–time-dependent velocity fluctuations that are consistent with the predicted mean flow and Reynolds stresses, thereby providing access to pressure statistics without the computational cost of scale-resolving simulations.

Table 1 Independent SST turbulence model parameters considered in the UQ workflow, together with nominal values and sampling intervals. The coefficients γ_1 and γ_2 are derived quantities and are not treated as independent uncertain parameters

Parameter	Description	Nominal value	Sampling interval
$\alpha_{\omega 1}$	ω diffusion coefficient (near-wall)	0.50	[0.30, 0.70]
$\alpha_{\omega 2}$	ω diffusion coefficient (outer layer)	0.856	[0.70, 1.00]
α_{k1}	k diffusion coefficient (near-wall)	0.85	[0.70, 1.00]
α_{k2}	k diffusion coefficient (outer layer)	1.00	[0.80, 1.20]
β_1	ω destruction coefficient (near-wall)	0.075	[0.06, 0.09]
β_2	ω destruction coefficient (outer layer)	0.0828	[0.07, 0.10]
β^*	k dissipation coefficient	0.09	[0.0784, 0.1024]
a_1	Eddy-viscosity limiter coefficient	0.31	[0.31, 0.40]
κ	von Kármán constant	0.41	[0.38, 0.42]
γ_1	Derived coefficient (near-wall)	Computed	Computed
γ_2	Derived coefficient (outer layer)	Computed	Computed

Starting from a Reynolds decomposition of the incompressible Navier–Stokes equations, the instantaneous pressure fluctuation p' satisfies a Poisson equation of the form

$$\nabla^2 p' = -\rho \left[\frac{\partial}{\partial x_i} \left(u'_j \frac{\partial \bar{u}_i}{\partial x_j} \right) + \frac{\partial^2}{\partial x_i \partial x_j} \left(u'_i u'_j - \overline{u'_i u'_j} \right) \right], \tag{10}$$

where $\bar{u}_i$ denotes the URANS mean velocity and u'_i the instantaneous velocity fluctuations. The mean velocity and Reynolds stresses appearing in (10) are obtained directly from URANS, while the fluctuating velocity field is constructed synthetically. AniPFM generates dimensionless velocity fluctuations using a spatial Fourier decomposition with a finite number of modes,

$$w_i(\mathbf{x}) = \sqrt{6} \sum_{n=1}^{N} \sqrt{q_n}\, \sigma_{in} \cos(\mathbf{k}_n \cdot \mathbf{x} + \varphi_n), \tag{11}$$

where the modal amplitudes q_n are distributed according to a modified von Kármán energy spectrum (Shur et al. 2014), the wavenumber vectors $\mathbf{k}_n$ span a mesh-dependent resolvable range, $\boldsymbol{\sigma}_n$ are divergence-free direction vectors with components σ_{in}, and φ_n are random phase shifts. This construction yields broadband, spatially correlated dimensionless velocity fluctuations.

Time dependence is introduced following the two-step procedure described in (Shur et al. 2014). First, the dimensionless velocity fluctuations are convected with the local URANS mean velocity. Second, temporal correlation is imposed through a combination of the convected field and a newly generated fluctuation field, with coefficients that enforce exponential decay of correlations. This yields space–time correlated fluctuations $v_i(\mathbf{x}, t)$ consistent with the turbulent time scales of the URANS solution.

Finally, anisotropy and physical scaling are imposed by transforming the space–time velocity fluctuations with the local Reynolds-stress tensor predicted by URANS,

$$u'_i = a_{ij} v_j, \qquad a_{ik} a_{kj} = R_{ij}, \tag{12}$$

where a_{ij} is obtained via a Cholesky decomposition of the Reynolds-stress tensor R_{ij}. This transformation ensures that the reconstructed velocity field reproduces the anisotropic Reynolds stresses of the underlying URANS solution.

By combining URANS mean-flow information with synthetic anisotropic velocity fluctuations, AniPFM provides pressure fluctuation fields that are consistent with the modeled turbulence dynamics while remaining computationally inexpensive. The model has been validated for canonical wall-bounded flows and TIV configurations (Zwijsen et al. 2024a, b) and forms a key enabling component of the present UQ framework.

In this study, AniPFM is used in conjunction with URANS for the channel-flow and annular-flow cases, enabling calibration and UQ of turbulence model parameters with respect to pressure-fluctuation-related QoIs. The AniPFM formulation is implemented and compiled within the OpenFOAM framework and is coupled to the URANS solver during the CFD simulations. All simulations presented in this work are performed using OpenFOAM, ensuring a consistent numerical environment across all flow configurations.

3 Results & discussion

This section presents the results of the proposed UQ framework applied to three flow configurations of increasing geometric and physical complexity: turbulent channel flow, turbulent annular flow, and a blunt-end cantilevered-rod configuration. The channel- and annular-flow cases serve as canonical, computationally affordable testbeds for global SA, surrogate verification, and Bayesian calibration, whereas the cantilevered-rod case represents a high-cost geometry representative of FIV applications.

For each configuration, the results are structured to highlight (i) the dominant turbulence model parameter sensitivities, (ii) the performance and consistency of the surrogate models, and (iii) the effect of Bayesian calibration on predictive uncertainty. The discussion focuses on identifying robust and transferable parameter trends across flow configurations, rather than reiterating methodological details introduced in Sect 2. Details on mesh resolution, wall-unit metrics, computational cost, and the total number of simulations performed for each case are summarized in Appendix A, providing context for the computational feasibility of the staged UQ strategy adopted in this study.

3.1 Channel flow case

Turbulent channel flow is considered as the first test case to assess the behaviour of the proposed UQ framework in a canonical wall-bounded configuration with available DNS reference data (Moser et al. 1999; Abe et al. 2001; Hoyas and Jiménez 2006). URANS–AniPFM simulations are performed at four friction Reynolds numbers, $Re_\tau = 180, 395, 640$, and 1020. SA is carried out at all four Reynolds numbers, while surrogate modelling and Bayesian calibration are performed for the reference case $Re_\tau = 640$. The computational setup and domain configuration are illustrated in Fig. 1.

3.1.1 Global sensitivity analysis

Figure 2 shows the first-order Sobol' sensitivity indices at $Re_\tau = 640$ for the pressure-fluctuation intensity p'^{+}_{rms} and the turbulent kinetic energy k as functions of the wall-normal coordinate y^+. Across both quantities, the dissipation coefficient β^* dominates the output variance throughout the channel, reflecting its central role in controlling the production–dissipation balance of the SST model and, through the URANS mean flow, the reconstructed pressure fluctuations. The coefficient $\alpha_{\omega 1}$ exhibits a consistent secondary influence, while κ and β_1 contribute primarily in the near-wall region. Although α_{k1} exhibits a localized sensitivity in the channel center region for k, its influence on the pressure-fluctuation intensity p'^{+}_{rms} remains negligible throughout the entire wall-normal range (Fig. 2). Its contribution to k also does not extend to the near-wall region and does not persist as a dominant parameter across Reynolds numbers (see Fig. 3). Since parameter reduction was guided by both the magnitude and spatial robustness of the sensitivity profiles, greater emphasis was placed on parameters exhibiting pronounced near-wall or Reynolds-number-consistent influence.

All remaining SST coefficients have negligible Sobol' indices over the entire wall-normal range. A corresponding analysis performed for the individual Reynolds-stress components $\overline{u'u'}^{+}$, $\overline{v'v'}^{+}$, and $\overline{w'w'}^{+}$ reveals virtually identical sensitivity distributions to those

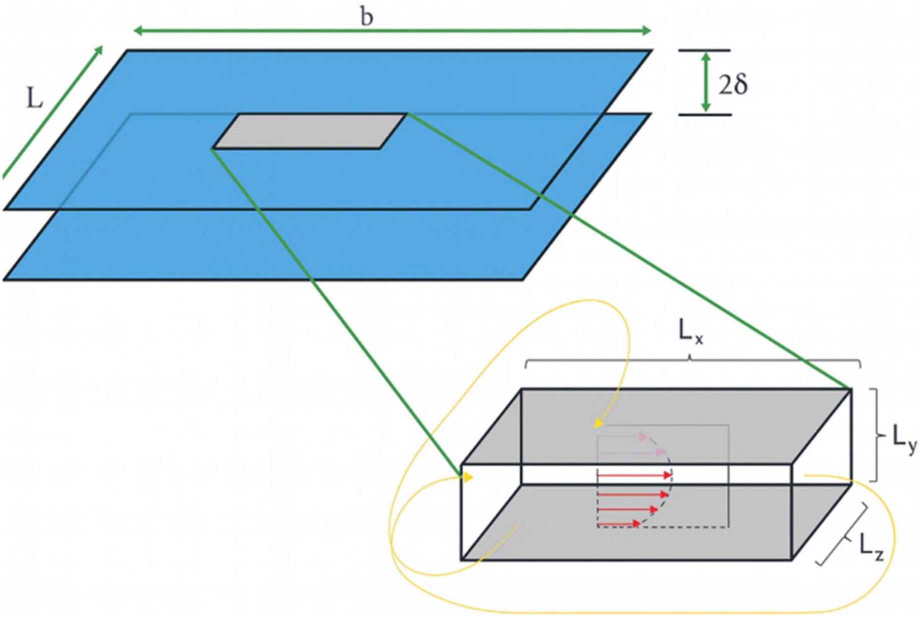

Fig. 1 Schematic representation of the turbulent channel-flow configuration. The upper panel shows the canonical two-plate channel, while the lower panel highlights the three-dimensional computational domain used in the simulations, including the periodic directions and mean-flow orientation

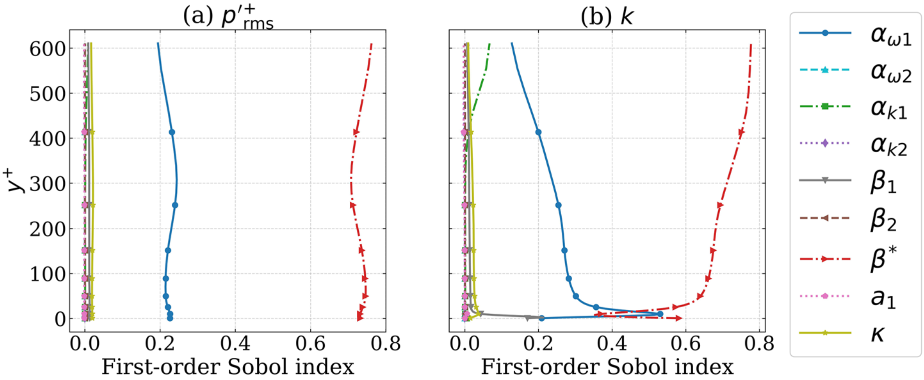

Fig. 2 First-order Sobol’ sensitivity indices for (**a**) pressure-fluctuation intensity prms′+ and (**b**) turbulent kinetic energy k as functions of the wall-normal location y+ at Reτ=640

of the turbulent kinetic energy k at all wall-normal locations. These results are therefore not shown separately.

The sensitivity structure is remarkably robust across Reynolds numbers. Figure 3 shows that, for all four Re_τ values, only four SST turbulence model parameters—β^*, $\alpha_{\omega 1}$, β_1 , and κ—exhibit non-negligible influence on the QoIs, while the remaining coefficients consistently contribute little to the output variance. Although the parameter ranking remains unchanged, a systematic variation in the magnitude of the Sobol’ indices is observed as the

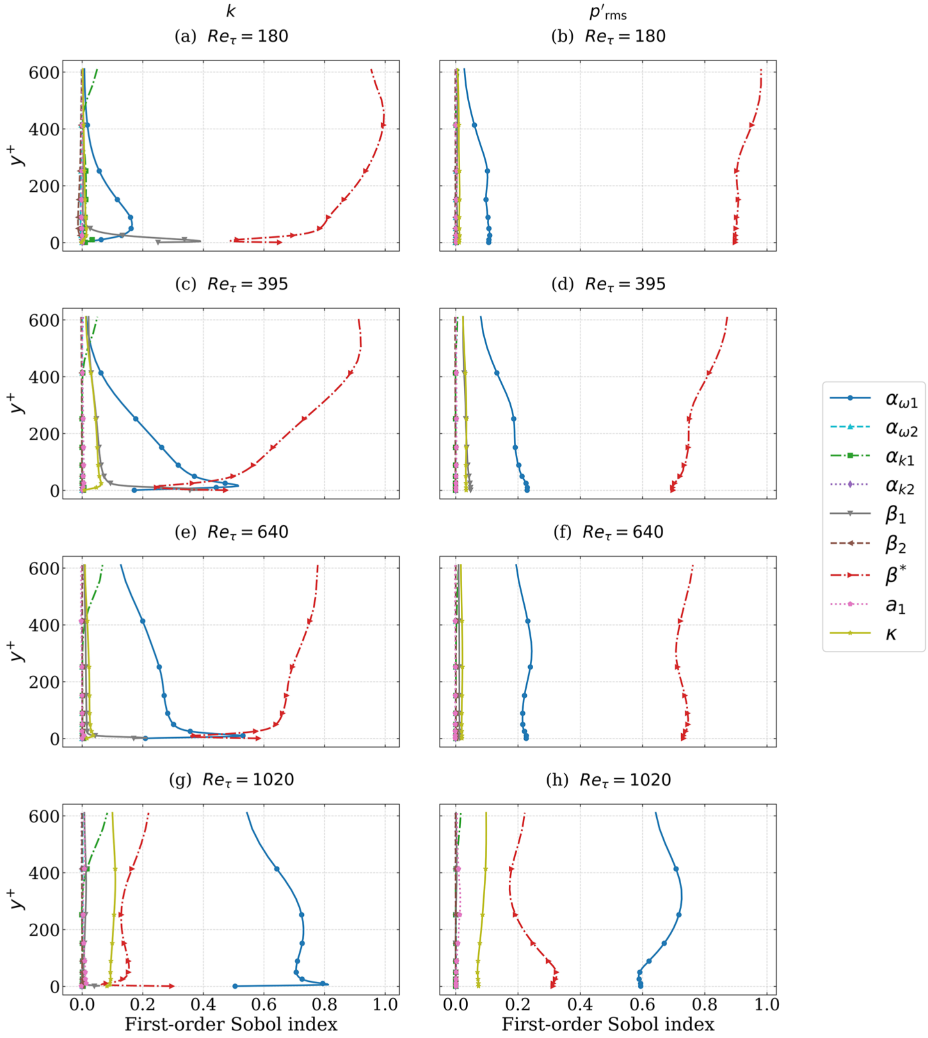

Fig. 3 First-order Sobol' sensitivity indices for the dominant SST turbulence model parameters at (**a,b**) Reτ=180, (**c,d**) Reτ=395, (**e,f**) Reτ=640, and (**g,h**) Reτ=1020. Results are shown as a function of wall-normal location y+ for turbulent kinetic energy and pressure-fluctuation intensity

Reynolds number increases. With increasing Re_τ, the sensitivity associated with $\alpha_{\omega 1}$ shifts toward larger values, whereas the contribution of β^* is progressively reduced. Importantly, the shape of the Sobol' profiles as a function of wall-normal location y^+ remains essentially unchanged across all Reynolds numbers, indicating that the same wall-normal sensitivity structure is preserved.

These trends indicate that increasing Re_τ primarily alters the relative importance of the dominant turbulence model parameters rather than the wall-normal regions in which they exert influence. The smooth and monotonic evolution of the Sobol' indices across successive Reynolds numbers, including the highest case $Re_\tau = 1020$ (subplots g,h), confirms that this behavior represents a continuous modulation of parameter influence rather than a qualitative change in sensitivity structure.

The Reynolds-number-invariant ranking of influential parameters motivates a reduction of the original nine-parameter SST model to a four-dimensional parameter space for all subsequent surrogate modeling and Bayesian calibration.

3.1.2 Surrogate verification

Gaussian-process surrogates are constructed in the reduced four-parameter space to emulate the URANS–AniPFM response. A surrogate-based SA is performed to assess whether the parametric dependencies of the original simulations are preserved. As illustrated in Fig. 4 for p'^{+}_{rms}, the surrogate reproduces both the dominant and negligible parameter contributions with high fidelity, confirming its suitability for Bayesian inference.

3.1.3 Bayesian calibration and predictive assessment

Bayesian calibration is performed at $Re_\tau = 640$ using DNS reference data for pressure fluctuations and Reynolds stresses. The resulting marginal posterior distributions (Fig. 5) show strong contraction of β^* and, to a lesser extent, $\alpha_{\omega 1}$, while β_1 and κ remain weakly informed. This posterior structure mirrors the sensitivity hierarchy identified by the Sobol' analysis.

Posterior predictive distributions are shown in Fig. 6. While the spanwise Reynolds stress and the near-wall pressure-fluctuation peak are reproduced with good accuracy, the streamwise and wall-normal Reynolds stresses remain poorly predicted. The narrow credible intervals indicate that these discrepancies are dominated by structural model-form limitations rather than parametric uncertainty.

Overall, the channel-flow case establishes a clear and Reynolds-number-invariant hierarchy among SST turbulence model parameters and highlights the intrinsic limits of parameter calibration in URANS-based turbulence modeling. These findings provide a reference for assessing parameter transferability in more complex configurations.

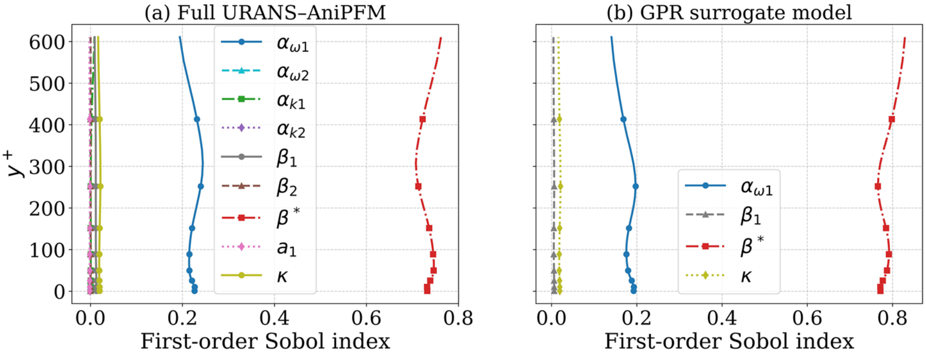

Fig. 4 Comparison of first-order Sobol' sensitivity indices for pressure-fluctuation intensity prms′ obtained from the full URANS–AniPFM simulations (left) and from the GPR surrogate (right)

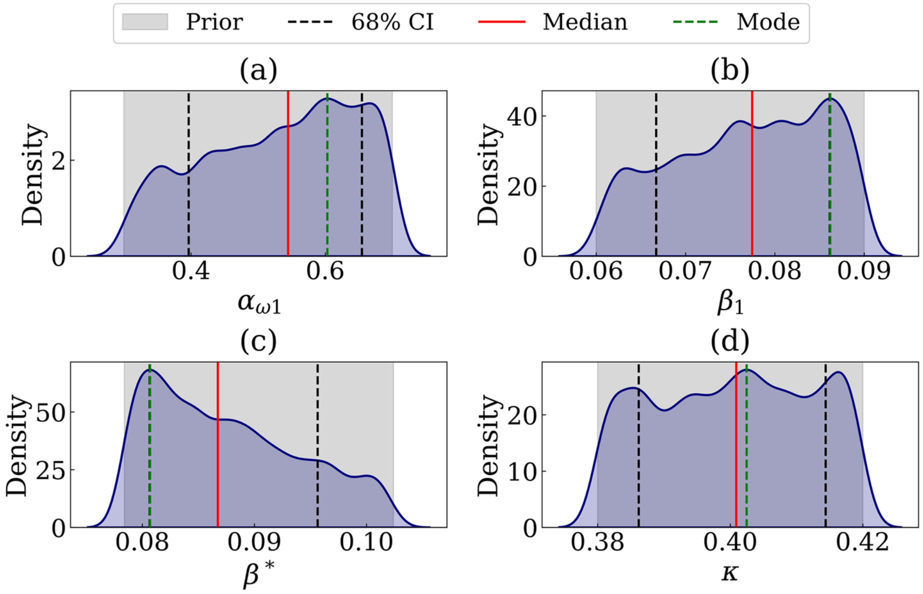

Fig. 5 Marginal posterior probability density functions of the calibrated SST turbulence model parameters for turbulent channel flow at Reτ=640: (**a**) αω1, (**b**) β1, (**c**) β*, and (**d**) κ. Shaded regions indicate the prior distributions, dashed black lines denote the 68% credible intervals, the red solid line marks the posterior median, and the green dashed line indicates the posterior mode

3.2 Annular flow case

The turbulent annular-flow configuration is considered as a second test case to examine the robustness of the inferred parameter trends in a curved, wall-bounded geometry representative of rod-bundle flows. The setup consists of an inner rod enclosed by an outer cylindrical wall and matches the configuration used for LES reference simulations in (Norddine and Benhamadouche 2023). A schematic of the geometry is shown in Fig. 7.

3.2.1 Global sensitivity analysis

Figure 8 shows the first-order Sobol' sensitivity indices for turbulent kinetic energy k and pressure-fluctuation intensity p'^{+}_{rms} as functions of the radial position. For both quantities, the variance is dominated by the dissipation coefficient β^* and the near-wall specific dissipation-rate coefficient $\alpha_{\omega 1}$ across the entire annular gap. Compared to the channel-flow case, the coefficient α_{k1} exhibits a more pronounced secondary influence on k, while the von Kármán constant κ contributes modestly in the central region of the annulus. All remaining SST model coefficients have negligible impact on the output variance. The Sobol' indices for turbulent kinetic energy show a clear dependence on radial position, reflecting the spatially varying role of individual turbulence model parameters in the curved, wall-bounded geometry. In contrast, the sensitivity indices associated with the pressure-fluctuation intensity remain nearly uniform across the annular gap. This indicates that, within the AniPFM-based reconstruction, pressure fluctuations depend primarily on global features of

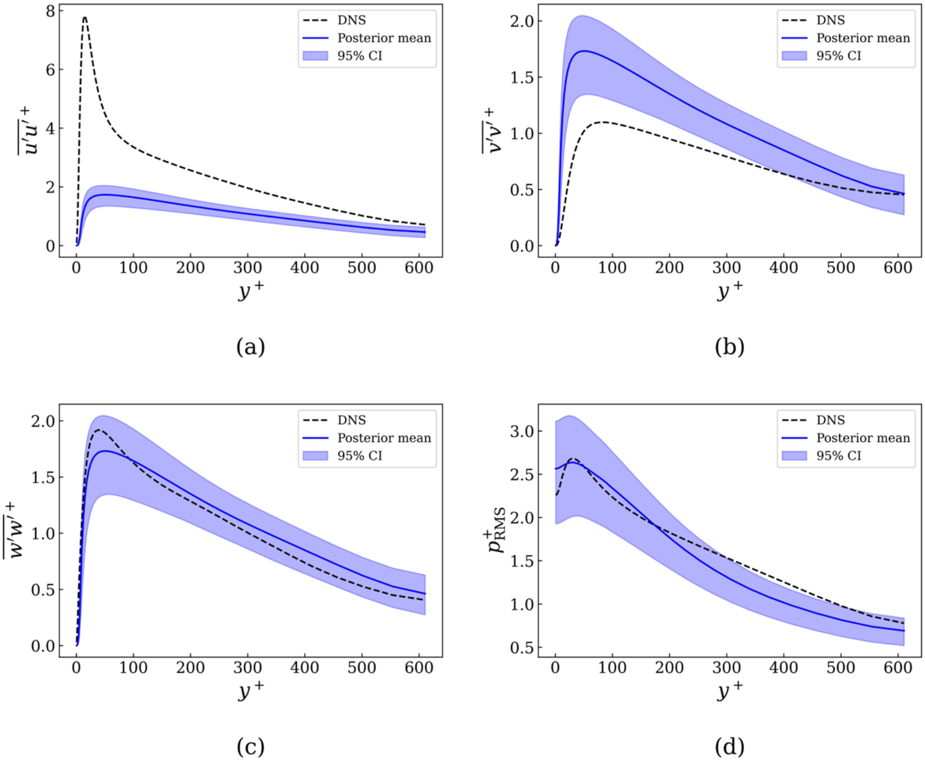

Fig. 6 Posterior predictive distributions for (**a**) streamwise Reynolds stress u′u′¯+, (**b**) wall-normal Reynolds stress v′v′¯+, (**c**) spanwise Reynolds stress w′w′¯+, and (**d**) pressure-fluctuation intensity prms′+ in turbulent channel flow at Reτ=640. Solid lines denote posterior means, shaded regions indicate 95% credible intervals, and dashed lines represent DNS reference data

Fig. 7 Schematic of the turbulent annular-flow configuration, showing the inner rod, outer wall, and axial flow direction

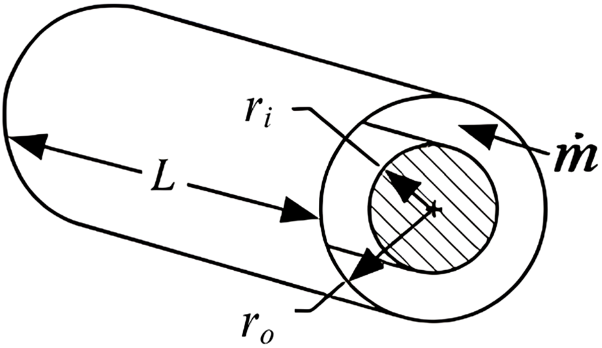

the URANS mean flow rather than on localized wall-normal variations of individual model parameters. A similar weak dependence of the pressure-fluctuation sensitivity indices on wall-normal location was observed in the turbulent channel-flow case, indicating that this behavior is consistent across geometries and intrinsic to the pressure-fluctuation modeling rather than specific to the annular configuration. Sensitivity results for the Reynolds-stress components exhibit the same parameter hierarchy as turbulent kinetic energy and are

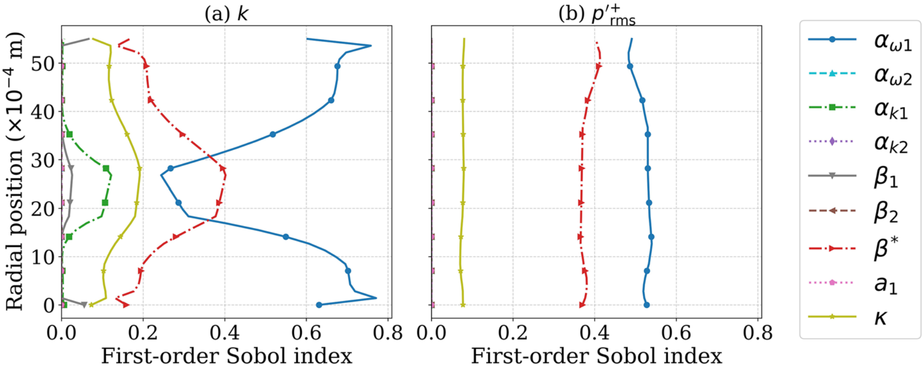

Fig. 8 First-order Sobol' sensitivity indices for turbulent annular flow: turbulent kinetic energy k (left) and pressure-fluctuation intensity prms′+ (right) as functions of radial position

therefore not shown. Similarly, surrogate-based sensitivity indices closely reproduce the URANS–AniPFM results, confirming that the identified parametric dependencies are not affected by surrogate approximation.

Overall, the annular-flow SA confirms that the effective dimensionality of the SST parameter space remains low. While $\alpha_{\omega 1}$ and β^* remain the dominant contributors, curvature effects redistribute the relative importance of secondary parameters, motivating a reduced four-parameter space for subsequent surrogate modeling and Bayesian calibration.

3.2.2 Surrogate modelling

Gaussian-process surrogates are constructed in the reduced parameter space $\boldsymbol{\theta} = (\alpha_{\omega 1}, \beta^*, \alpha_{k1}, \kappa)$ to emulate the URANS–AniPFM response. The surrogates are trained for 160 scalar outputs, including mean streamwise velocity, turbulent kinetic energy, and Reynolds stresses (wall-normal and streamwise) evaluated at 40 radial locations. Validation and leave-one-out diagnostics indicate uniformly low prediction errors, supporting their use for Bayesian inference.

3.2.3 Bayesian calibration

Bayesian calibration is performed using LES reference data (Norddine and Benhamadouche 2023) for turbulent kinetic energy and Reynolds stresses. The resulting marginal posterior distributions are shown in Fig. 9. In contrast to the channel-flow case, all four parameters exhibit only weak posterior contraction relative to their priors, indicating limited identifiability in the annular geometry.

This behavior is consistent with the sensitivity results: although a reduced subset of parameters dominates the variance, their overall influence on the annular-flow quantities is weaker than in channel flow, limiting the information content of the LES data for parameter identification.

3.2.4 Posterior predictive assessment

Posterior predictive distributions are shown in Fig. 10. The mean streamwise velocity is predicted with high confidence, exhibiting narrow credible intervals and close agreement with

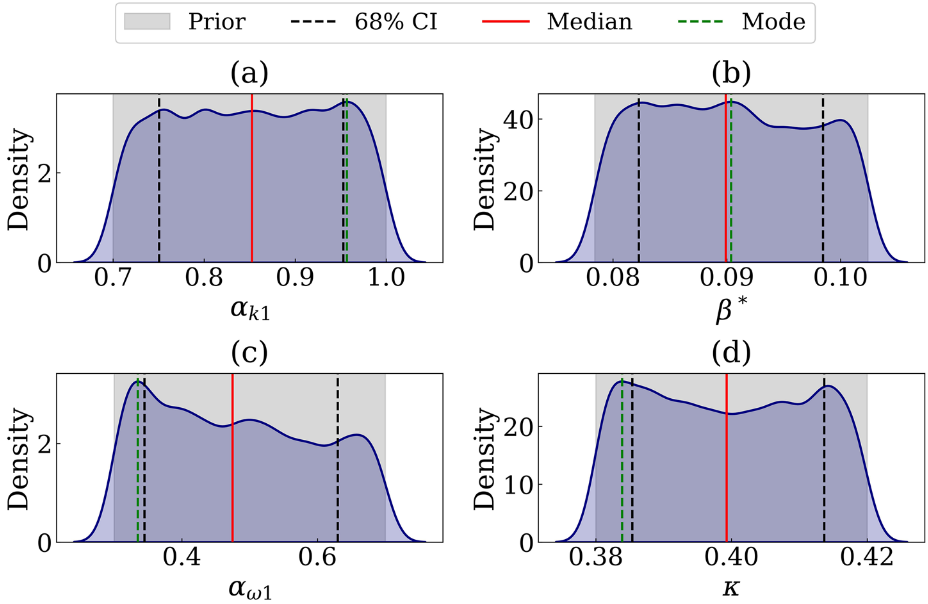

Fig. 9 Marginal posterior probability density functions of the calibrated SST turbulence model parameters for turbulent annular flow: (**a**) αk1, (**b**) β*, (**c**) αω1, and (**d**) κ. Shaded regions indicate the prior distributions, dashed black lines denote the 68% credible intervals, the red solid line marks the posterior median, and the green dashed line indicates the posterior mode

LES data. In contrast, the predictive envelopes for turbulent kinetic energy and Reynolds stresses remain broad and do not fully bracket the reference profiles.

The persistence of prediction error despite calibration indicates that, for annular flow, discrepancies between URANS–AniPFM and LES are dominated by structural model-form limitations rather than parametric uncertainty.

3.3 Cantilevered-rod case

The third test case considers turbulent axial flow around a cantilevered cylindrical rod with a blunt end, representative of configurations relevant to FIV. Unlike the channel- and annular-flow cases, this geometry is computationally expensive, making large-scale parameter exploration infeasible. The analysis therefore targets uncertainty in SST turbulence model parameters that govern mean-flow quantities relevant for subsequent FSI simulations (Fig. 11).

The rod and outer channel diameters are $D_i = 0.011$ m and $D_o = 0.021$ m, respectively. A bulk inlet velocity of $U_{\mathrm{bulk}} = 3.45$ m/s is prescribed, matching the operating conditions of the wall-resolved LES reference data. Velocity and turbulent kinetic energy profiles are extracted at six axial stations downstream of the blunt end. Among these, three near-tip locations (P2–P4) are selected for Bayesian calibration, where turbulence–structure interaction effects are most pronounced. The probe locations follow the definition used in the LES study of Norddine and Benhamadouche (2023) (Table 2).

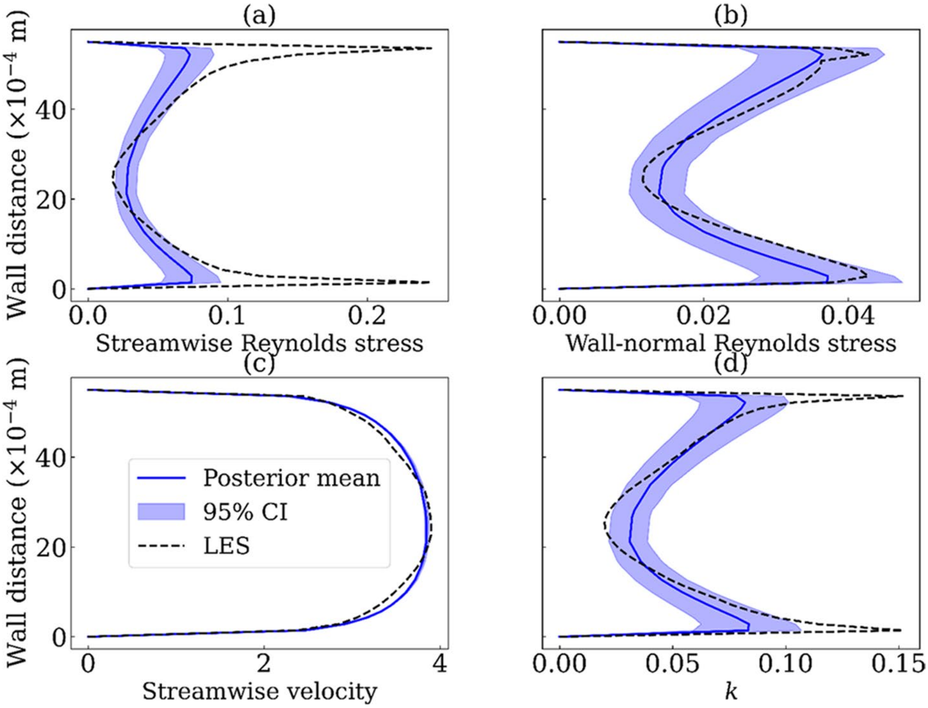

Fig. 10 Posterior predictive distributions for turbulent annular flow: (**a**) streamwise Reynolds stress, (**b**) wall-normal Reynolds stress, (**c**) mean streamwise velocity, and (**d**) turbulent kinetic energy. Solid lines denote posterior means, shaded regions indicate 95% credible intervals, and dashed lines represent LES reference data

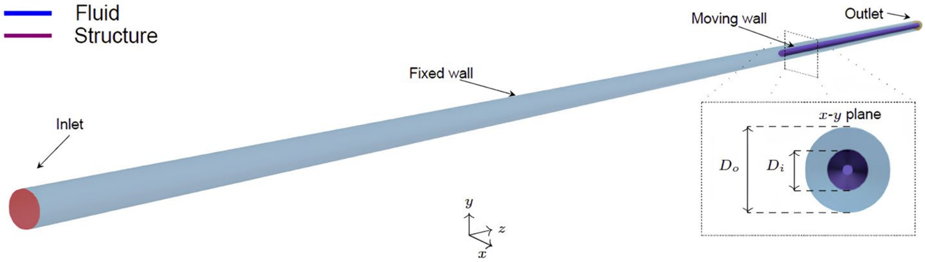

Fig. 11 Computational geometry of the cantilevered-rod configuration. Flow enters from the free tip side and exits near the clamped end

Table 2 Axial locations of the profile extraction stations measured from the start of the blunt end

Station	P1	P2	P3	P4	P5	P6
z (m)	5.0×10^{-4}	4.0×10^{-3}	8.0×10^{-3}	2.0×10^{-2}	1.0×10^{-1}	2.0×10^{-1}

3.3.1 Parameter reduction and surrogate construction

Global Sobol' SA is not performed for the cantilevered-rod configuration due to the prohibitive cost of repeated URANS simulations. Instead, parameter-ranking information obtained from the turbulent channel- and annular-flow cases is transferred to this geometry. Across both auxiliary flows, the SST dissipation coefficient β^* and the near-wall specific dissipation-rate coefficient $\alpha_{\omega 1}$ consistently emerged as the dominant contributors to output variability. These two parameters are therefore retained as the only uncertain inputs for the rod-case analysis.

Restricting the surrogate input space to $\{\alpha_{\omega 1}, \beta^*\}$ reduces the dimensionality of the problem and lowers the number of required CFD simulations by more than an order of magnitude, rendering surrogate construction computationally feasible. A total of 65 URANS simulations are performed using an LHS design in the reduced parameter space. Two surrogate-modeling approaches are constructed using the same training dataset. GPR is employed as the primary surrogate for Bayesian calibration, while PCE is used to assess robustness with respect to surrogate formulation. For the PCE surrogate, the polynomial degree is selected via cross-validation, with a total degree of $p = 3$ providing the best compromise between accuracy and numerical stability.

Although AniPFM is not coupled to the URANS simulations for this case, a single verification run confirms that including AniPFM does not affect the mean velocity or turbulent kinetic energy profiles used for surrogate construction. This justifies the URANS-only formulation adopted here and avoids the exponential increase in computational cost associated with long URANS–AniPFM transients.

3.3.2 Bayesian calibration

Bayesian calibration is performed using LES reference data (Norddine and Benhamadouche 2023) at stations P2–P4. Figure 12 shows the marginal posterior distributions obtained using the GPR surrogate. Both parameters exhibit clear contraction relative to their uniform priors, indicating successful parameter identification despite the reduced sampling budget.

Posterior distributions inferred using the PCE surrogate (Fig. 13) closely match the GPR-based results, with consistent modes and credible intervals. This agreement demonstrates that the inferred parameter trends are robust with respect to the choice of surrogate model.

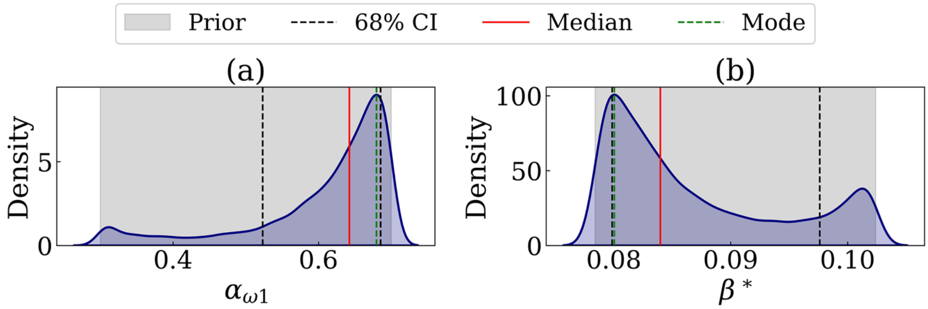

Fig. 12 Marginal posterior distributions of αω1 and β* for the cantilevered-rod case obtained using the GPR surrogate. Shaded regions denote 68% credible intervals

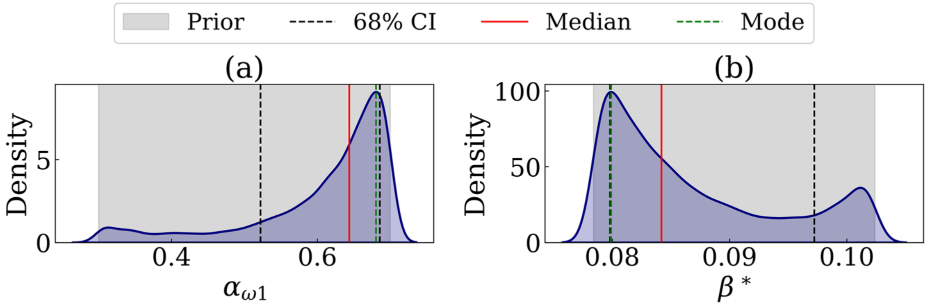

Fig. 13 Marginal posterior distributions of αω1 and β* for the cantilevered-rod case obtained using the PCE surrogate

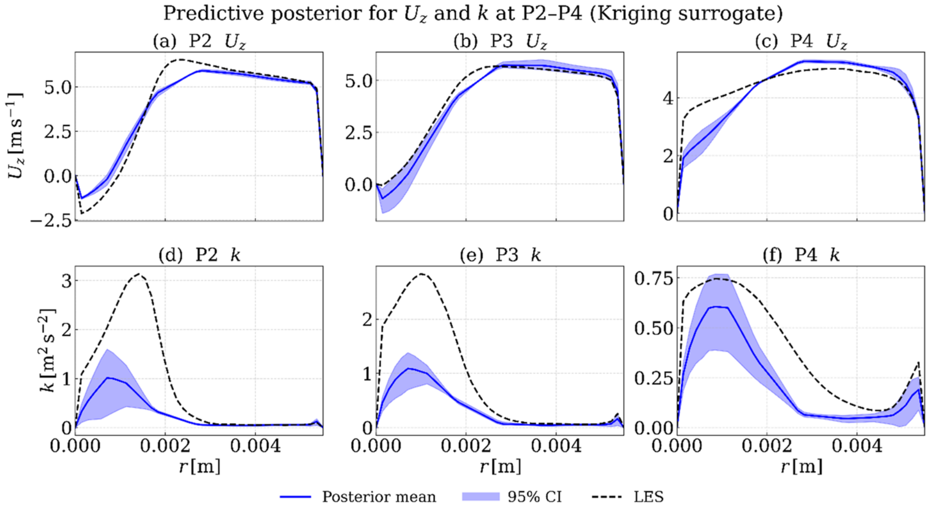

Fig. 14 Posterior predictive distributions for the cantilevered-rod case obtained using the GPR surrogate. Streamwise velocity Uz(**r**) (top row) and turbulent kinetic energy k(**r**) (bottom row) are shown at probe locations P2–P4

3.3.3 Posterior predictive assessment

Posterior predictive distributions are obtained by propagating posterior samples through the surrogate models. Figure 14 shows the GPR-based posterior means and 95% credible intervals together with LES reference data at stations P2–P4.

The posterior mean reproduces the qualitative shape of the streamwise velocity profiles, but the LES data lie outside the 95% credible intervals over substantial portions of the radial domain. For turbulent kinetic energy, the posterior mean significantly underpredicts the LES results at all probe locations, and the predictive intervals fail to enclose the reference profiles. The relatively narrow uncertainty bands indicate that these discrepancies are dominated by structural model-form error rather than parametric uncertainty.

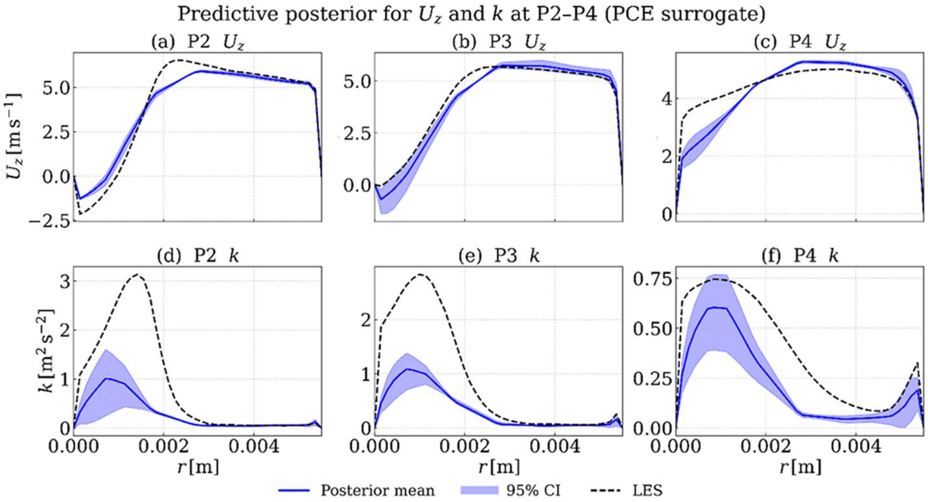

Fig. 15 Posterior predictive distributions for the cantilevered-rod case obtained using the PCE surrogate. Notation and layout are identical to the GPR-based results

Posterior predictive distributions obtained using the PCE surrogate (Fig. 15) are nearly indistinguishable from the GPR-based results and lead to identical conclusions regarding model limitations and uncertainty structure.

3.4 Cross-case discussion

The turbulent channel-flow and annular-flow configurations act as computationally inexpensive canonical analogues of the cantilevered-rod case. While these auxiliary flows do not reproduce the geometric complexity of the rod tip, they capture the dominant wall-bounded shear mechanisms governing mean-flow development, turbulence production, and near-wall anisotropy. Their role within the present study is therefore to establish robust and transferable turbulence model parameter hierarchies prior to calibration on the substantially more expensive rod geometry.

For turbulent channel flow, global SAs conducted over a wide range of friction Reynolds numbers ($Re_\tau = 180, 395, 640, 1020$) consistently identify the same subset of influential SST parameters: β^*, $\alpha_{\omega 1}$, β_1, and κ. Importantly, both the composition and the relative ranking of this subset are invariant with respect to Reynolds number, indicating that the observed sensitivity structure reflects intrinsic properties of the SST closure rather than flow-specific operating conditions.

The annular-flow configuration exhibits a closely related sensitivity hierarchy. Here, β^* and $\alpha_{\omega 1}$ again dominate the variance of all QoIs, while α_{k1} and κ play secondary roles. Although curvature effects alter the relative importance of second-order contributors, the repeated dominance of β^* and $\alpha_{\omega 1}$ across both auxiliary geometries provides a clear and physically consistent basis for reducing the parameter space in the cantilevered-rod case to these two coefficients.

The Bayesian calibration results reinforce this cross-case consistency. In the channel-flow case, parameters identified as influential by the global SA—most notably β^* and $\alpha_{\omega 1}$

—are strongly constrained by the data, whereas parameters with negligible Sobol' indices retain broad, prior-like posterior distributions. This direct correspondence confirms that the channel-flow data contain sufficient information to identify the dominant turbulence model coefficients.

In contrast, the annular-flow case exhibits weaker parameter identifiability, with posterior distributions remaining comparatively broad. Despite this, posterior predictive distributions show good agreement with the LES reference data, indicating that remaining discrepancies are dominated by structural model limitations rather than parametric uncertainty. This behavior highlights that predictive accuracy and parameter identifiability need not coincide and depend strongly on the underlying flow physics.

For the cantilevered-rod configuration, Bayesian calibration of the reduced two-parameter model again yields well-informed posterior distributions for $\alpha_{\omega 1}$ and β^*, despite the substantially higher computational cost and reduced sampling budget. The contraction of these parameters toward regions consistent with the auxiliary-flow results confirms that the dominant parameter hierarchy identified in simpler geometries transfers reliably to the FSI-relevant rod case.

From a computational perspective, the staged strategy adopted in this work yields substantial efficiency gains. Performing full-dimensional SA on the auxiliary flows eliminates the need for prohibitively expensive exploration of the high-dimensional parameter space in the rod configuration. Reducing the surrogate input space from nine parameters to two makes surrogate-based Bayesian inference tractable and enables posterior sampling using inexpensive surrogate evaluations rather than repeated high-fidelity CFD simulations.

Across all configurations considered, $\alpha_{\omega 1}$ and β^* consistently emerge as the dominant contributors to variability in mean-flow quantities and turbulent kinetic energy. This conclusion holds despite methodological differences between cases, including the use of AniPFM-based fluctuation reconstruction in the auxiliary flows and URANS-only simulations for the rod geometry. In all cases, Bayesian calibration shifts $\alpha_{\omega 1}$ toward larger values within its admissible range and β^* toward smaller values, indicating a robust and physically interpretable correction to the turbulence transport and dissipation balance.

The calibrated values obtained for the cantilevered-rod case therefore provide a physically consistent parameter set for subsequent simulations of similar FSI-relevant configurations. At the same time, the results clarify the scope of turbulence-model calibration within eddy-viscosity closures relying on the Boussinesq approximation. While Bayesian inference reduces parametric uncertainty and improves consistency across configurations, residual deviations from high-fidelity data persist due to structural assumptions inherent in linear eddy-viscosity modeling, including constrained representation of stress anisotropy and simplified pressure–strain redistribution. As such, parameter calibration alone cannot fully recover flow features governed by these structural limitations. More advanced closures, such as Reynolds Stress Models, nonlinear eddy-viscosity formulations, or hybrid RANS–LES approaches, may offer improved representation at the expense of increased computational complexity. The present framework therefore aims to deliver uncertainty-aware predictions within the practical constraints of URANS-based modeling rather than to eliminate intrinsic structural deficiencies.

4 Conclusions

This work presented a scalable and computationally efficient framework for global SA, surrogate modeling, and Bayesian calibration of turbulence model parameters in wall-bounded turbulent flows. By combining inexpensive canonical configurations with targeted calibration on a high-cost geometry, the approach enables UQ in settings where direct, brute-force strategies would be computationally infeasible.

Global SA performed on turbulent channel-flow and turbulent annular-flow configurations revealed a clear and robust hierarchy among SST turbulence model parameters. Across multiple geometries and Reynolds numbers, the specific dissipation rate coefficient $\alpha_{\omega 1}$ and the turbulent kinetic energy dissipation coefficient β^* consistently emerged as the dominant contributors to model variability. The cantilevered-rod case confirmed the transferability of this hierarchy, with Bayesian calibration constraining these same parameters toward consistent regions of the admissible parameter space, despite the substantially higher computational cost.

Surrogate modeling played a central role in enabling Bayesian inference. GPR and PCE surrogates produced consistent posterior distributions and predictive uncertainty estimates, demonstrating that the inferred parameter trends are robust with respect to surrogate formulation. This robustness is essential for practical deployment of surrogate-based UQ in complex flow configurations.

The results further demonstrate both the capabilities and the limitations of turbulence model calibration. While Bayesian inference substantially reduces parametric uncertainty in wall-bounded flows, persistent discrepancies with high-fidelity reference data indicate that structural model-form uncertainty can dominate once the most influential parameters are calibrated. This finding underscores the need to complement parameter calibration with advanced modeling strategies, such as Reynolds Stress Models (RSMs) or scale-resolving approaches, when accurate prediction of complex turbulent flows is required. The transferability observed across channel, annular, and rod configurations suggests robustness of the identified parameter hierarchy within wall-bounded shear flows. However, extension to flows involving stronger curvature, pronounced three-dimensionality, or significant flow-history effects would require additional validation and, if necessary, re-evaluation of dominant parameter sets.

Overall, the proposed multistage framework provides a practical and physically grounded route for turbulence model UQ in engineering-relevant geometries. By exploiting transferable sensitivity information from canonical flows and leveraging surrogate-based inference, the methodology enables robust calibration at a computational cost compatible with large-scale applications, including flows relevant to FSI.

Appendix A

Computational cost and mesh resolution

Table A1 in the Supplementary Material summarizes the mesh resolution, near-wall grid spacing, and computational cost for all simulations performed in the UQ workflow. For each configuration, the table reports the mesh level used, the total number of cells, characteristic wall-unit resolution, CPU cost per CFD run, and the total number of simulations executed. SA and surrogate-model training employ different mesh levels where appropriate to balance accuracy and computational cost.

For the channel-flow case, a structured hexahedral mesh is used with uniform spacing in the homogeneous directions and wall-normal stretching to ensure $y^+_{\mathrm{avg}} \lesssim 1$. The mesh characteristics reported in Table A1 correspond to the reference case $Re_\tau = 640$, for which a mesh-sensitivity study was conducted.

For the annular-flow case, a structured cylindrical mesh is employed. SA simulations are carried out on a coarse mesh with an average radial wall-unit resolution $r^+_{\mathrm{avg}} \approx 1.2$, while surrogate-model training uses a medium mesh with $r^+_{\mathrm{avg}} \approx 0.85$ to improve the accuracy of reconstructed turbulence quantities. Here, r^+ denotes the wall-normal distance from the solid surfaces expressed in viscous units.

For the cantilevered-rod case, all simulations are performed on a coarse structured hexahedral mesh containing approximately 1.9×10^6 cells. The near-wall resolution at the rod surface is characterized by $r^+_{\mathrm{inner,avg}} \approx 0.85$, while the axial resolution near the rod tip is quantified by $z^+_{\mathrm{tip,avg}} \approx 24$. These metrics ensure adequate resolution of mean-flow and turbulence quantities relevant for downstream FIV analyses.

Mesh-sensitivity studies were performed for all three configurations to verify that the selected resolutions provide mesh-independent predictions of the QoIs. For brevity, detailed mesh-convergence results are not reported here.

Based on the number of simulations and per-run CPU costs reported in Table A1, the total computational expense of the uncertainty-quantification study is approximately 2×10^5 CPU hours. All simulations were performed using domain-decomposed, parallelized OpenFOAM solvers. For the turbulent channel-flow and annular-flow configurations, each URANS simulation was executed using 8 CPU cores, reflecting their comparatively modest computational requirements. In contrast, the cantilevered-rod simulations were substantially more expensive and were therefore run using 48 CPU cores per case. This difference in core count is reflected in both the wall-clock time per simulation and the overall computational cost distribution.

All computations were performed on the DelftBlue high-performance computing system at Delft University of Technology, provided by the Delft High Performance Computing Centre (DHPC 2024). Simulations were executed using parallel OpenFOAM solvers on Intel-based compute nodes interconnected via a high-bandwidth InfiniBand network.

The majority of the total computational cost arises from the cantilevered-rod configuration, highlighting the necessity of the staged workflow adopted in this study. By exploiting inexpensive canonical flows to perform global sensitivity analysis and parameter reduction, the dimensionality of the calibration problem for the high-cost geometry is significantly reduced, rendering surrogate-based Bayesian inference computationally feasible.

Supplementary Information The online version contains supplementary material available at https://doi.org/10.1007/s10494-026-00763-x.

Acknowledgements The authors acknowledge the use of DelftBlue computational resources provided by the Delft High Performance Computing Centre. The authors also thank Kevin Zwijsen, Sina Tajfirooz, and Alexander von Zuijlen for providing CFD test cases and access to the AniPFM implementation used in this study.

Author contributions A. E.: Conceptualization (equal); Methodology (equal); Software & code (lead); Formal analysis (lead); Writing – original draft (lead). R. P. D.: Conceptualization (equal); Methodology (equal); Supervision (lead); Writing – review and editing (equal).

Funding A. E. acknowledges support from the GO-VIKING project (Grant No. 101060826) under the Euratom Research and Training Programme.

Data availability The data used in the current study are available from the authors on reasonable request.

Declarations

Competing interests The authors declare no competing interests.

References

Abe, H., Kawamura, H., Matsuo, Y.: Direct numerical simulation of a fully developed turbulent channel flow with respect to the Reynolds number dependence. J. Fluids Eng. **123**(2), 382–393 (2001). https://doi.org/10.1115/1.1366680

Cheung, S.H., Oliver, T.A., Prudencio, E.E., Prudhomme, S., Moser, R.D.: Bayesian uncertainty analysis with applications to turbulence modeling. Reliab. Eng. Syst. Saf. **96**(9), 1137–1149 (2011). https://doi.org/10.1016/j.ress.2010.09.013

Da Ronch, A., Panzeri, M., Drofelnik, J., d'Ippolito, R.: Sensitivity and calibration of turbulence model in the presence of epistemic uncertainties. CEAS Aeronaut. J. **11**(1), 33–47 (2020). https://doi.org/10.1007/s13272-019-00389-y

De Ridder, J., Degroote, J., Van Tichelen, K., Schuurmans, P., Vierendeels, J.: Modal characteristics of a flexible cylinder in turbulent axial flow from numerical simulations. J. Fluids Struct. **43**, 110–123 (2013). https://doi.org/10.1016/j.jfluidstructs.2013.09.001

Delft High Performance Computing Centre (DHPC): DelftBlue Supercomputer (Phase 2). https://www.tudelft.nl/dhpc/ark:/44463/DelftBluePhase2 (2024)

Di Stefano, M.A., Hosder, S., Baurle, R.A.: Effect of turbulence model uncertainty on scramjet strut injector flow field analysis. Comput. & Fluids **229**, 105104 (2021). https://doi.org/10.1016/j.compfluid.2021.105104

Duraisamy, K., Iaccarino, G., Xiao, H.: Turbulence modeling in the age of data. Annu Rev Fluid Mech. **51**(1), 357–377 (2019). https://doi.org/10.1146/annurev-fluid-010518-040547

Edeling, W.N., Cinnella, P., Dwight, R.P., Bijl, H.: Bayesian estimates of parameter variability in the k–ε turbulence model. J. Comput. Phys. **258**, 73–94 (2014)

Eidi, A., Ghiassi, R., Yang, X., Abkar, M.: Model-form uncertainty quantification in RANS simulations of wakes and power losses in wind farms. Renew. Energy **179**, 2212–2223 (2021). https://doi.org/10.1016/j.renene.2021.08.012

Eidi, A., Zehtabiyan-Rezaie, N., Ghiassi, R., Yang, X., Abkar, M.: Data-driven quantification of model-form uncertainty in Reynolds-averaged simulations of wind farms. Phys. Fluids **34**(8) (2022). https://doi.org/10.1063/5.0100076

Erb, A.J., Hosder, S.: Uncertainty analysis of turbulence model closure coefficients for shock wave-boundary layer interaction simulations. In: 2018 AIAA Aerospace Sciences Meeting, pp. 2077. (2018)

Georgiadis, N., Yoder, D.: Recalibration of the shear stress transport model to improve calculation of shock separated flows. In: 51st AIAA Aerospace Sciences Meeting Including the New Horizons Forum and Aerospace Exposition, pp. 685. (2013)

Ghanem, R.G., Spanos, P.D.: Spectral stochastic finite-element formulation for reliability analysis. J. Eng. Mech. **117**(10), 2351–2372 (1991). https://doi.org/10.1061/(ASCE)0733-9399(1991)117:10(2351)

Haario, H., Saksman, E., Tamminen, J.: An adaptive metropolis algorithm. Bernoulli. **7**(2), 223–242 (2001). https://doi.org/10.2307/3318737

Herman, J., Usher, W.: Salib: an open-source Python library for sensitivity analysis. JOSS **2**(9), 97 (2017). https://doi.org/10.21105/joss.00097

Hosder, S., Walters, R., Balch, M.: Efficient sampling for non-intrusive polynomial chaos applications with multiple uncertain input variables. In: 48th AIAA/ASME/ASCE/AHS/ASC Structures, Structural Dynamics, and Materials Conference, pp. 1939. (2007)

Hosder, S., Walters, R.W., Balch, M.: Point-collocation nonintrusive polynomial chaos method for stochastic computational fluid dynamics. Aiaa J. **48**(12), 2721–2730 (2010). https://doi.org/10.2514/1.39389

Hoyas, S., Jiménez, J.: Scaling of the velocity fluctuations in turbulent channels up to Reτ= 2003. Phys. Fluids **18**(1) (2006)

Jp, L., Zeng, F., Chen, S., Zhang, K., Yan, C.: Bayesian model evaluation of three k–ω turbulence models for hypersonic shock wave–boundary layer interaction flows. Acta Astronaut. **189**, 143–157 (2021)

Kennedy, M.C., O'Hagan, A.: Bayesian calibration of computer models. J. Educ. Chang. R. Stat. Soc.: Ser. B (Stat. Methodol.). **63**(3), 425–464 (2001). https://doi.org/10.1111/1467-9868.00294

Kottapalli, S., Sharma, S., Shams, A., Zuijlen, A., Pourquie, M.: Numerical simulation of turbulence induced vibrations from URANS models using the pressure fluctuation model. In: 17th International Topical Meeting on Nuclear Reactor Thermal Hydraulics, NURETH 2017 Association for Computing Machinery (ACM). (2017)

Li, J., Chen, S., Cai, F., Wang, S., Yan, C.: Bayesian uncertainty analysis of SA turbulence model for supersonic jet interaction simulations. Chin. J. Aeronaut. **35**(4), 185–201 (2022). https://doi.org/10.1016/j.cja.2021.07.039

Margheri, L., Meldi, M., Salvetti, M.V., Sagaut, P.: Epistemic uncertainties in RANS model free coefficients. Comput. & Fluids **102**, 315–335 (2014). https://doi.org/10.1016/j.compfluid.2014.06.029

McKay, M.D., Beckman, R.J., Conover, W.J.: A comparison of three methods for selecting values of input variables in the analysis of output from a computer code. Technometrics **42**(1), 55–61 (2000). https://doi.org/10.1080/00401706.2000.10485979

Menter, F.R.: Two-equation eddy-viscosity turbulence models for engineering applications. Aiaa J. **32**(8), 1598–1605 (1994). https://doi.org/10.2514/3.12149

Moser, R.D., Kim, J., Mansour, N.N., et al.: Direct numerical simulation of turbulent channel flow up to Reτ=590. Phys. Fluids **11**(4), 943–945 (1999). https://doi.org/10.1063/1.869966

Norddine, T., Benhamadouche, S.: Wall-resolved LES and URANS simulations of an axial flow on a cantilevered rod at a moderate Reynolds number. In: 20th International Topical Meeting on Nuclear Reactor Thermal Hydraulics (NURETH-20), American Nuclear Society (ANS), Washington, DC (2023)

Oliver, T.A., Moser, R.D.: Bayesian uncertainty quantification applied to RANS turbulence models. J. Phys. Conf. Ser. **318**(4), 042032 (2011). https://doi.org/10.1088/1742-6596/318/4/042032. IOP Publishing

Qiu, X., Wen, Y., Zhou, X., Liu, Y.: Bayesian calibration of RANS model parameters based on hybrid surrogate modeling and adaptive sampling. Comput. Fluids **308**, 106982 (2026). https://doi.org/10.1016/j.compfluid.2026.106982

Saltelli, A., Ratto, M., Andres, T., Campolongo, F., Cariboni, J., Gatelli, D., et al.: Global sensitivity analysis: the primer. John Wiley & Sons (2008)

Schaefer, J., Hosder, S., West, T., Rumsey, C., Carlson, J.R., Kleb, W.: Uncertainty quantification of turbulence model closure coefficients for transonic wall-bounded flows. AIAA J. **55**(1), 195–213 (2017). https://doi.org/10.2514/1.J054902

Shu, Y., Wu, J., Yang, Y., Zhao, Z.: Fretting wear and fatigue life analysis of fuel bundles subjected to turbulent axial flow in CEFR. Sci. Technol. Nucl. Install. (1), 1–11 (2019). https://doi.org/10.1155/2019/5613737

Shur, M.L., Spalart, P.R., Strelets, M.K., Travin, A.K.: Synthetic turbulence generators for RANS-LES interfaces in zonal simulations of aerodynamic and aeroacoustic problems. Flow Turbul. Combust. **93**(1), 63–92 (2014). https://doi.org/10.1007/s10494-014-9534-8

Smirnov, A., Shi, S., Celik, I.: Random flow generation technique for large eddy simulations and particle-dynamics modeling. J. Fluids Eng. **123**(2), 359–371 (2001). https://doi.org/10.1115/1.1369598

Subbian, G., Botelho e Souza, A.C., Radespiel, R., Zander, E., Friedman, N., Moshagen, T., et al.: Calibration of an extended eddy viscosity turbulence model using uncertainty quantification. In: AIAA Scitech 2020 Forum, p. 1031. (2020)

Williams, C.K., Rasmussen, C.E.: Gaussian processes for machine learning, vol. 2. MIT press, Cambridge, MA (2006)

Xiao, H., Cinnella, P.: Quantification of model uncertainty in RANS simulations: a review. Prog. Aerosp. Sci. **108**, 1–31 (2019). https://doi.org/10.1016/j.paerosci.2018.10.001

Xiu, D., Karniadakis, G.E.: Modeling uncertainty in steady state diffusion problems via generalized polynomial chaos. Comput. Methods Appl. Mech. Eng. **191**(43), 4927–4948 (2002). https://doi.org/10.1016/S0045-7825(02)00421-8

Zhang, K., Zhao, Y., Wang, Q., Li, J.-P., Zeng, F., Yan, C.: Uncertainty analysis and calibration of SST turbulence model for free shear layer in cavity-ramp flow. Acta Astronaut. **192**, 168–181 (2022). https://doi.org/10.1016/j.actaastro.2021.12.027

Zhao, Y., Liu, H., Yan, C.: Uncertainty quantification of k-ω turbulence model for hypersonic flow. In: 2018 9th International Conference on Mechanical and Aerospace Engineering (ICMAE), pp. 526–530. IEEE (2018)

Zhao, Y., Yan, C., Wang, X., Liu, H., Zhang, W.: Uncertainty and sensitivity analysis of SST turbulence model on hypersonic flow heat transfer. Int. J. Heat Mass Transf. **136**, 808–820 (2019). https://doi.org/10.1016/j.ijheatmasstransfer.2019.03.012

Zwijsen, K., Marreiros de Freitas, A., Tajfirooz, S., Frederix, E., van Zuijlen, A.: An optimized anisotropic pressure fluctuation model for the simulation of turbulence-induced vibrations. Phys. Fluids **36**(12) (2024a). https://doi.org/10.1063/5.0235792

Zwijsen, K., van den Bos, N., Frederix, E., Roelofs, F., van Zuijlen, A.: Development of an anisotropic pressure fluctuation model for the prediction of turbulence-induced vibrations of fuel rods. Nucl. Eng. Des. **425**, 113316 (2024b). https://doi.org/10.1016/j.nucengdes.2024.113316